

# Consideration of artificial compressibility for explicit computational fluid dynamics simulation

kazuma, nagata

Interdisciplinary Graduate School of Engineering Sciences, Kyushu University

Ikegaya, Naoki

Interdisciplinary Graduate School of Engineering Sciences, Kyushu University

Tanimoto, Jun

Interdisciplinary Graduate School of Engineering Sciences, Kyushu University

<https://hdl.handle.net/2324/4751322>

---

出版情報 : Journal of Computational Physics. 443 (110524), 2021-10-15. Academic Press  
バージョン :  
権利関係 :



Title: Consideration of artificial compressibility for explicit computational fluid dynamics  
simulation

Authors:

K. Nagata<sup>a</sup>, N. Ikegaya<sup>a,b</sup>, and J. Tanimoto<sup>a,b</sup>

Affiliations:

<sup>a</sup> Interdisciplinary Graduate School of Engineering Sciences, Kyushu University, Japan

<sup>b</sup> Faculty of Engineering Sciences, Kyushu University, Japan

Corresponding author:

K. Nagata

Kasuga-koen 6-1, Kasuga-shi, Fukuoka 816-8580, Japan

+81-092-583-7644

[nagata.kazuma@kyudai.jp](mailto:nagata.kazuma@kyudai.jp)

Abstract:

In this paper, we discuss the theoretical interpretation of the artificial compressibility method (ACM) to propose a new explicit method for the unsteady numerical simulation of fluid flow. The proposed method employs the compressible continuity and Navier–Stokes equations, which facilitates the replacement of pressure as one of the major variables with density, theoretically backed by virtual particle concept. This new concept justifies the theoretical treatment assuming the speed of sound in ACM as a model parameter determined by the grid system. More importantly, the present method realizes, in a fully explicit manner, the solving of a set of equations, which prevents the solving of the Poisson equation of pressure. The new method was validated and proven by comparing the results of two-dimensional cavity flow between the proposed method, conventional incompressible method, and the Lattice–Boltzmann method with varying Reynolds numbers (100, 1000, and 10000). The results of the proposed method agree well with conventional and reference data for both steady-state and unsteady-state conditions, although slight numerical oscillations were observed for the proposed method at a Reynolds number of 10000. Thus, the numerical validation assures that the proposed method is an explicit method based on a solid theoretical ground to be a new efficient simulation framework.

Keywords: Explicit computational fluid dynamics simulation, virtual particle, computational fluid dynamics, cavity flow

## 1. Introduction

Most computational fluid dynamics (CFD) simulations of air flow under low Mach conditions assume incompressible fluids because the compressibility of fluid is negligible for velocity fields. This assumption also means that the change in internal energy by dissipation and work by compression and expansion is not necessary to consider for such determination of the air flow. However, this also requires coupling the continuity and Navier–Stokes equations to determine the pressure  $p$  that inevitably requires solving the Poisson equation by an iterative numerical procedure, which accounts for the majority of computational load of such a conventional framework presuming ‘incompressible fluid’.

To avoid solving the Poisson equation of  $p$ , several technical procedures have been proposed earlier. For example, Chorin [1] proposed a new algorithm known as the artificial compressibility method (ACM), in which some degree of artificial compressibility is considered despite dealing with an incompressible fluid. Technically, ACM replaces the speed of sound  $a$  with an arbitrary model parameter. This allows the method to solve the temporal evolution of  $p$  without an iteration process. Although ACM was originally aimed at solving a steady flow field of incompressible fluid with high numerical efficiency, some studies have reported that ACM can be applied for unsteady flow fields [2–4]. Additionally, modified ACMs have also been proposed as a numerically effective and stable method. Accordingly, Clausen [5] interpreted ACM as a compressible fluid with an isentropic process based on the theoretical equation of  $p$ . Additionally, they proposed an entropically damped artificial compressibility method (EDACM), which can reduce the acoustic wave propagation that causes temporal and spatial oscillations. EDACM replaced the temperature diffusion with pressure diffusion to reduce unfavorable oscillations in  $p$  and velocity  $\mathbf{u}$ . Ansumali et al. [6] proposed the kinetically reduced local Navier–Stokes equations (KRLNS), which establishes the simplified the pressure equation based on the grand potential instead of the entropy as the suitable thermodynamic potential. Borok et al. [7] conduct numerical simulations of two-dimensional cavity flow and two-dimensional Taylor–Green vortex flow to compare the results of the KRLNS and ACM. In addition, Toutant [8] proposed the general pressure equation (GPE), which the pressure equation is derived by the budget equation of the enthalpy, and compared them [9]. In the field of marine engineering, the technical approach of compressible CFD methods is also studied. For example, Bigay et al. [10] proposed a weakly-compressible cartesian hydrodynamic (WCCH) solver, which the pressure equation is based on the polytropic equation of state. All of these methods have the Eulerian governing equations such as Navier–Stokes equations, which means they describe the fluid motion on the macroscopic scale. On the other hand, the Lattice–Boltzmann method (LBM) [11] has been focused in various wind engineering fields. It solves the lattice Boltzmann equation, which means that it describes the flow motion on the mesoscopic scale. He et al. [12] compared LBM and ACM in detail to consider the relationship between them.

However, as mentioned above, several CFD methods have been proposed, we focus on ACM and EDACM in this study. Although these precursors successfully proved that their artificial compressible framework is applicable in solving incompressible fluid flows explicitly, the speed of sound  $a$  is determined by the arbitrary model parameter. Alternatively, these methods must be understood as technical procedures to solve problems regarding incompressible fluids numerically with an artificial parameter. As a result, both ACM and EDACM require the quantification of artificial parameter in numerical procedures, as reported in previous studies [13–17].

Motivated by the above background, we report a theoretical consideration accounting for incompressible fluids into an unsteady simulation framework, presuming a fully explicit method wherein a new idea relying on the virtual particle concept is introduced. The virtual



particles are conceptually ideal, that are introduced in the LBM; however, the proposed method still retains the Eulerian governing equations, namely, the continuity and Navier–Stokes equations. The proposed method is compared with the conventional CFD method (Simplified Marker-And Cell method, or SMAC) [18], LBM, and that employed in a previous study by Ghia et al. [19] for a two-dimensional cavity flow to justify the applicability of the proposed method, named as the explicit method with the virtual particle concept (EMV).

This study is organized as follows: the theoretical background of EMV is explained in Section 2, the velocity fields of the cavity flow are discussed in Section 3, and the conclusive remarks are provided in Section 4.

## 2. Theory

### 2.1 Governing equations

We start from the theoretical budget equations for a compressible fluid to consider the physical interpretation of artificial compressibility approaches (e.g., ACM and EDACM). The continuity and Navier–Stokes equations for a compressible fluid can be written as

$$\frac{\partial \rho}{\partial t} + u_j \frac{\partial \rho}{\partial x_j} = -\rho\theta, \quad (2.1.1)$$

$$\rho \frac{\partial u_i}{\partial t} + \rho u_j \frac{\partial u_i}{\partial x_j} = -\frac{\partial p}{\partial x_i} + \frac{\partial}{\partial x_j} (\lambda \theta \delta_{ij} + \mu e_{ij}). \quad (2.1.2)$$

Here, variables are defined as follows;  $t$ : time [s],  $x_i$ : the coordinate for the  $i$ -th direction [m],  $u_i$ : the velocity for the  $i$ -th component [m/s],  $p$ : the pressure [Pa],  $\rho$ : the fluid density [kg/m<sup>3</sup>],  $\mu$ : the dynamic viscosity [kg/ms],  $\lambda$ : the second dynamic viscosity [kg/ms],  $e_{ij} = (\partial u_j / \partial x_i + \partial u_i / \partial x_j)$ : the velocity strain tensor,  $\delta_{ij}$ : the Kronecker's delta, and  $\theta = \partial u_i / \partial x_i$ : the divergence of the velocity.

For an ideal gas, where  $\rho$  can be expressed by two independent microstate variables,  $p$  and temperature  $T$ ,  $\rho = \rho(p, T)$ . Hence, the total derivative of  $\rho$  with respect to  $t$  gives the equation of  $p$  as follows:

$$\frac{D\rho}{Dt} = \left(\frac{\partial \rho}{\partial p}\right)_T \frac{Dp}{Dt} + \left(\frac{\partial \rho}{\partial T}\right)_p \frac{DT}{Dt}. \quad (2.1.3)$$

Here,  $D/Dt = \partial/\partial t + u_j \partial/\partial x_j$ , and the suffix of  $T$  or  $p$  indicates the partial derivative with fixing  $T$  or  $p$ , respectively. By employing the continuity equation, the budget equation of internal energy, and the ideal gas equation ( $p/\rho = RT$ , where  $R$  is the gas constant [J/kgK]), we obtain

$$\frac{Dp}{Dt} = (\gamma - 1) \left( k \frac{\partial^2 T}{\partial x_j \partial x_j} + \phi \right) - \gamma p \theta. \quad (2.1.4)$$

Here,  $k$  is the thermal conductivity [J/Kms],  $\phi$  is the dissipation rate of the kinetic energy of the fluid per volume [J/m<sup>3</sup>s], and  $\gamma = c_p/c_v$  is the ratio of the specific heat ( $c_p$ : the specific heat with the isobaric condition [J/kgK], and  $c_v$  is the specific heat with isochoric condition [J/kgK]).

We consider how Eq. (2.1.4) is expressed for isothermal, isentropic, and isochoric conditions.

For an ideal gas, the internal energy budget equation is written as follows:

$$\rho c_v \frac{DT}{Dt} = k \frac{\partial^2 T}{\partial x_j \partial x_j} + \phi - p\theta. \quad (2.1.5)$$

The isothermal condition means that  $DT/Dt = 0$  and  $\partial T / \partial x_j = 0$ ; therefore, we obtain  $\phi = p\theta$ , meaning that the entire reduction of kinetic energy owing to the dissipation, balances with work, by the pressure and volume expansion. Because the speed of sound  $a$  is defined as

$$a^2 = \frac{\partial p}{\partial \rho}, \quad (2.1.6)$$

we can rewrite Eq. (2.1.4) under isothermal conditions by substituting  $\phi = p\theta$  and  $a^2 = p/\rho$  as follows.

$$\frac{Dp}{Dt} = -p\theta = -a^2 \rho \theta. \quad (2.1.7)$$

For an isentropic condition, the specific entropy  $s$  [J/kgK], expressed by

$$\rho T \frac{Ds}{Dt} = k \frac{\partial^2 T}{\partial x_j \partial x_j} + \phi, \quad (2.1.8)$$

is kept constant. Therefore, we obtained  $Ds/Dt = 0$ , or RHS=0. By substituting  $a^2 = \gamma p/\rho$ , we obtain.

$$\frac{Dp}{Dt} = -\gamma p \theta = -a^2 \rho \theta, \quad (2.1.9)$$

which is identical to Eq. (2.1.7).

Eqs. (2.1.7) and (2.1.9) are identical because both the isothermal and isentropic conditions are categorized as barotropic flow, where  $p = p(\rho)$ . Therefore, the simple chain rule  $Dp/Dt = (D\rho/Dt)(dp/d\rho)$  gives the following  $p$  equation:

$$\frac{Dp}{Dt} = -a^2 \rho \theta, \quad (2.1.10)$$

with Eq. (2.1.6). Therefore, the  $p$  equation for both barotropic conditions is identically expressed by using  $a$ ,  $\rho$ , and  $\theta$ . Eq. (2.1.10) is considered to be employed as a basic equation for the original ACM [1], although they have not mentioned the physical meaning of the governing equation. We recall the interpretation of Eq. (2.1.10), with several assumptions applied in the ACM in Section 2.2.1.

For the isochoric condition, we can assume that  $D\rho/Dt = 0$  in Eq. (2.1.3). Hence, we obtain,

$$T = \frac{\gamma}{\rho c_p (\gamma - 1)} p. \quad (2.1.11)$$

Substitution of Eq. (2.1.11) to Eq. (2.1.5) gives

$$\frac{Dp}{Dt} = \alpha \gamma \frac{\partial^2 p}{\partial x_j \partial x_j} + (\gamma - 1) \phi - \gamma p \theta. \quad (2.1.12)$$

Here,  $\alpha = k/\rho c_p$  [m<sup>2</sup>/s] is the thermal diffusivity. Eq. (2.1.12) is the original form of  $p$  in the equation used in EDACM [5], although they did not mention their assumption as the isochoric condition. Under this condition,  $a$  cannot be defined since  $a^2 = \partial p / \partial \rho \rightarrow \infty$  theoretically. However, we nominally denote  $p = a^2 \rho$ . By substituting  $a$  and taking the condition of  $a \rightarrow \infty$ , we obtain

$$\lim_{a \rightarrow \infty} \rho \theta = \lim_{a \rightarrow \infty} \frac{1}{\gamma a^2} \left( \alpha \gamma \frac{\partial^2 p}{\partial x_j \partial x_j} + (\gamma - 1) \phi - \frac{Dp}{Dt} \right) = 0. \quad (2.1.13)$$

This means that the isochoric condition is identical with the incompressible assumption.

Based on the equations of  $p$  in Eq. (2.1.10) for the barotropic condition, and Eq. (2.1.12) for the isochoric condition, we discuss the premise and assumptions used in ACM and EDACM in the following section.

## 2.2 Artificial compressibility approach

### 2.2.1. ACM by Chorin (1967) [1]

The original ACM proposed by Chorin [1] employed the following two assumptions: i) a substantial derivative of  $p$  can be expressed as  $Dp/Dt \sim \partial p / \partial t$ , and ii)  $a$  is a model parameter (or artificial speed of sound) satisfying  $p = a^2 \rho$ . These assumptions give the following  $p$  equation:

$$\frac{\partial p}{\partial t} = -a^2 \rho \theta. \quad (2.2.1)$$

Therefore, employing ACM indicates that the following set of equations is solved.

$$\frac{\partial \rho}{\partial t} = -\rho \theta, \quad (2.2.2)$$

$$\frac{\partial u_i}{\partial t} + u_j \frac{\partial u_i}{\partial x_j} = -\frac{a^2}{\rho} \frac{\partial \rho}{\partial x_i} + \frac{1}{\rho} \frac{\partial}{\partial x_j} (\lambda \theta \delta_{ij} + \mu e_{ij}). \quad (2.2.3)$$

According to these equations, we discuss the physical meaning and interpretation of ACM. First, the conventional ACM is used as a numerical technique to solve an incompressible flow problem under steady-state conditions with an arbitrary parameter  $a$ . As seen, the difference in Eq. (2.1.1), and Eq. (2.2.2), the mass conservation cannot be satisfied under the unsteady-state condition in ACM. Therefore, we have to interpret that Eq. (2.2.2) satisfies the physical constraint of continuity only when  $\partial \rho / \partial t = 0$ . In other words,

extending the ACM for solving an unsteady flow development is not theoretically appropriate. Alternatively, Eq. (2.2.1) is physically reasonable even under an unsteady state if the advection term of  $p$  (i.e.,  $u_j \partial p / \partial x_j$ ) remains the same as Eq. (2.1.10) for both barotropic flow conditions. This means that we should solve the set of equations in Eq. (2.1.10), and Eq. (2.2.3) for the unsteady-state flow. Secondly, Clausen (2013) [5] explains that ACM is one of the limitations with isentropic assumption; however, both isothermal and isentropic (i.e., barotropic conditions) give the same  $p$  equation as in Eq. (2.1.7), and Eq. (2.1.9). Therefore, the conventional ACM must be interpreted as barotropic flow under the assumption of  $u_j \partial_j p = 0$ . The last aspect is the selection of  $a$ . We can understand that its preferable to replace the value of  $a$  by an artificial speed of sound, that's less than its realistic speed in terms of numerical procedure for both  $\rho$  and  $u_i$  because the characteristic speeds of the system are expressed as  $u_i$  and  $u_i \pm a$  from the eigenvalues of the coefficient matrix of the governing equations. However, the aforementioned derivation of the set of equations for the ACM does not explain why we can assume  $a$  as an arbitral model parameter.

## 2.2.2. EDACM by Clausen (2013) [5]

Clausen (2013) [5] introduced EDACM as a method that minimizes the density fluctuation. When  $\rho = \rho(p, T)$ , the total derivative of  $\rho$  is

$$d\rho = \left(\frac{\partial \rho}{\partial T}\right)_p dT + \left(\frac{\partial \rho}{\partial p}\right)_T dp. \quad (2.2.4)$$

If we assume that  $d\rho \sim 0$  as employed in the EDACM, we obtain

$$dp = -\left(\frac{\partial \rho}{\partial T}\right)_p \left(\frac{\partial \rho}{\partial p}\right)_T^{-1} dT = \rho c_p \left(1 - \frac{1}{\gamma}\right) dT. \quad (2.2.5)$$

The integral of Eq. (2.2.5) leads to Eq. (2.1.11), meaning that the assumption in EDACM is identical to the isochoric or incompressible condition, although Clausen (2013) [5] did not mention this aspect. In addition, the EDACM assumes that i)  $\phi = 0$ , and ii)  $a^2 = \gamma p / \rho$ . When these assumptions are applied to Eq. (2.1.12), the  $p$  equation in EDACM is written as

$$\frac{Dp}{Dt} = \alpha \gamma \frac{\partial^2 p}{\partial x_j \partial x_j} - a^2 \rho \theta. \quad (2.2.6)$$

Hence, applying EDACM indicates that the following set of equations is solved.

$$\frac{\partial \rho}{\partial t} + u_j \frac{\partial \rho}{\partial x_j} = -\rho \theta - \frac{\phi}{T c_v}, \quad (2.2.7)$$

$$\frac{\partial u_i}{\partial t} + u_j \frac{\partial u_i}{\partial x_j} = -\frac{a^2}{\gamma \rho} \frac{\partial \rho}{\partial x_i} + \frac{1}{\rho} \frac{\partial}{\partial x_j} (\lambda \theta \delta_{ij} + \mu e_{ij}). \quad (2.2.8)$$

Similarly, the mass conservation is not achieved in EDACM because of the difference in Eq. (2.2.7), and Eq. (2.2.1). Additionally, the physical interpretation of Eq. (2.2.7) is not clear. Moreover, EDACM must be interpreted as an isochoric (incompressible) condition because minimizing  $d\rho$  is absolutely required. However, the condition is satisfied only when  $a^2 = \partial p / \partial \rho \rightarrow \infty$ . Nonetheless, the parameter  $a$  appears in Eq. (2.2.8) as an arbitrary model parameter. Furthermore, the derivation of equations for EDACM does not explain why  $a$  can be a model parameter.

To summarize the problems in artificial compressible approach, firstly mass conservation is not satisfied theoretically, and secondly the speed of sound  $a$  can be selected as an arbitrary model parameter that is also not explained theoretically. We think that both aspects are not critical issues in terms of solving the fluid dynamics numerically, based on ACM and EDACM, as previous researchers have justified the accuracy of these methods by comparing the conventional numerical method [4,14]. However, theoretical understanding is required to reason, why these assumptions allow us to derive the fluid dynamics motion numerically, based on artificial compressibility equation with parameter  $a$ .

## 2.3 Interpretation of parameter $a$

### 2.3.1. General theory of kinetic energy of gases

To provide a theoretical interpretation to assume  $a$  as the model parameter in ACM and EDACM, we consider the fundamental definition of the pressure by molecule motions. Given that a mono-atomic molecule  $i$  of  $n$  [mol] with mass  $m$  [kg/pcs], the velocity  $\mathbf{q}^i$  [m/s], the total internal energy  $U$  [J] is

$$U = 0.5m\sum_i^{nN_A} \mathbf{q}^i{}^2 = 0.5mq_T^2 nN_A, \quad (2.3.1)$$

where  $N_A$  is Avogadro number, by taking the summation of the total number of molecules  $nN_A$  [pcs].  $q_T$  is the root mean squared speed of molecules, or the thermal velocity, which is written as

$$q_T^2 = \frac{1}{nN_A} \sum_i^{nN_A} \mathbf{q}^i{}^2 = \frac{\int_{-\infty}^{\infty} f(\mathbf{q}) \mathbf{q}^2 d\mathbf{q}}{\int_{-\infty}^{\infty} f(\mathbf{q}) d\mathbf{q}}. \quad (2.3.2)$$

Here,  $f(\mathbf{q})$  is the Maxwell distribution for molecules with respect to velocity  $\mathbf{q}$  [m/s]. Eq. (2.3.1) is also written as

$$U = \frac{0.5}{D} m \sum_i^{nN_A} q_x^i{}^2 \quad (for D) = \begin{cases} 0.5m\sum_i^{nN_A} q_x^i{}^2 & (for 1D) \\ 0.5m\sum_i^{nN_A} (q_x^i{}^2 + q_y^i{}^2) & (for 2D) \\ 0.5m\sum_i^{nN_A} (q_x^i{}^2 + q_y^i{}^2 + q_z^i{}^2) & (for 3D) \end{cases}. \quad (2.3.3)$$

Because of the homogeneity of molecules in each direction for dimension  $D$ . Here,  $q_x^i, q_y^i$  and  $q_z^i$  represent the velocity component in  $x, y, z$  and direction of  $\mathbf{q}^i$ , respectively.

Meanwhile since molecule motions are given by a change in momentum in one direction per unit area:

$$p = m\sum_i^N q_x^i{}^2. \quad (2.3.4)$$

Here,  $N$  [pcs/m<sup>3</sup>] is the molecular density per unit volume ( $=nN_A/\Omega$  [pcs/m<sup>3</sup>], where  $\Omega$  [m<sup>3</sup>] is the fluid volume). By multiplying  $\Omega$ , we obtain

$$p\Omega = m\sum_i^{nN_A} q_x^i{}^2. \quad (2.3.5)$$

Therefore, the following relationship for  $U$  and  $p$  for D-dimensional gas can be obtained:

$$p\Omega = \frac{2U}{D} = \frac{mq_T^2 nN_A}{D}. \quad (2.3.6)$$

We call Eq. (2.3.6) the general form of Bernoulli's theorem for D-dimensional gas. By dividing  $\Omega$ ,  $p$  can be written as:

$$p = \rho \frac{q_T^2}{D}, \quad (2.3.7)$$

where  $\rho = nN_A m / \Omega$  [kg/m<sup>3</sup>] is the total number of molecules multiplied by the mass per volume. This indicates that pressure is given by thermal velocity  $q_T$  defined by the total mean internal energy of molecules.

### 2.3.2. Explicit method with virtual particle concept (EMV)

On introduction of the concept of virtual particles, by grouping molecules of number  $E$ , the particle will have a velocity  $\mathbf{q}_v^i$ , where  $i$  represents an index to express the  $i$ -th virtual particle ( $i = 1$  to  $nN_A/E$ ). The virtual particle can move from one point to another, defined by a lattice grid with uniform grid length of  $\Delta$  during a representative time scale  $\Delta t$ . The motion to diagonal neighboring grids, such as the length of  $\sqrt{2}\Delta$  and  $\sqrt{3}\Delta$ , is also possible depending on considering ultra-discretization, which means the discretization of the dependent variables. In this context, velocity of the molecules is discretized as  $\mathbf{c}_i$  ( $i = 0$  to  $M$ , where  $M$  is the number of discretized velocities). Examples of the lattice grid are given in Appendix A1.

By following the definition and derivation of  $U$  and  $p$  based on the theory of kinetic energy of gases, we can define the internal energy  $U_v$  and pressure  $p_v$  by the virtual particles as follows:

$$U_v = 0.5m_v \sum_i^{nN_A/E} \mathbf{q}_v^i{}^2 = 0.5m_v q_{vT}^2 \frac{nN_A}{E} = 0.5m q_{vT}^2 nN_A. \quad (2.3.8)$$

Here,  $m_v = mE$  [kg] is the mass of virtual particle with  $E$  a molecule. The root mean squared velocity of the virtual particle,  $q_{vT}$ , is

$$q_{vT}^2 = \frac{E}{nN_A} \sum_i^{nN_A/E} \mathbf{q}_v^i{}^2 = \frac{\sum_{i=0}^M f_i \mathbf{c}_i^2}{\sum_{i=0}^M f_i}. \quad (2.3.9)$$

Here,  $f_i$  ( $i = 0$  to  $M$ ) is the distribution function of the virtual particle.  $f_i$  and  $\mathbf{c}_i$  are determined once the lattice grid for the discretization is defined (please refer to Appendix A1). If we assume that the distribution of virtual particle is homogenous in each  $D$  direction, we obtain

$$U_v = \frac{0.5}{D} m_v \sum_i^{nN_A/E} q_{vx}^i{}^2. \quad (2.3.10)$$

Here,  $q_{vx}^i$  represents the x-component of  $\mathbf{q}_v^i$ . The pressure  $p_v$  due to virtual particle motions is given by a change in the momentum in one direction per unit area as:

$$p_v = m_v \sum_i^{N/E} q_{vx}^i{}^2. \quad (2.3.11)$$

Here,  $N/E$  [pcs/m<sup>3</sup>] is the virtual particle density per unit volume ( $=nN_A/E\Omega$ ). By multiplying  $\Omega$ , we obtain

$$p_v \Omega = m_v \sum_i^{nN_A/E} q_{vx}^i{}^2. \quad (2.3.12)$$

Therefore, the following relationship is obtained for  $U_v$  and  $p_v$  for  $D$  dimensional flow:

$$p_v \Omega = \frac{2U_v}{D} = \frac{m_v q_{vT}^2 nN_A}{DE} = \frac{m q_{vT}^2 nN_A}{D}. \quad (2.3.13)$$

By dividing Eq. (2.3.13) by  $\Omega$ ,

$$p_v = \rho_v \frac{q_{vT}^2}{D} = \rho \frac{q_{vT}^2}{D}. \quad (2.3.14)$$

Here,  $\rho_v = (m_v nN_A)/E\Omega = mnN_A/\Omega = \rho$  [kg/m<sup>3</sup>] is the fluid density. This is  $\rho = \rho_v$  because the total mass does not change when the molecules or virtual particles are accounted for.

From Eqs. (2.3.8) and (2.3.14), the following relationships are obtained:

$$U_v = U \frac{q_{vT}^2}{q_T^2}, \quad (2.3.15)$$

$$p_v = p \frac{q_{vT}^2}{q_T^2}. \quad (2.3.16)$$

Therefore,  $U_v$  and  $p_v$  are smaller than those determined by kinematic energies of molecules. This is because the virtual particle is defined as a group of  $E$  molecules, indicating that internal energy within the group is not accounted for by  $U_v$  and  $p_v$ . When we denote these differences as  $\Delta U_v$  and  $\Delta p_v$ ,  $U$  and  $p$  are written as

$$\begin{aligned} U &= U_v + \Delta U_v \\ &= 0.5m_v q_{vT}^2 \frac{nN_A}{E} + \Delta U_v, \end{aligned} \quad (2.3.17)$$

$$\begin{aligned} p &= p_v + \Delta p_v \\ &= \frac{\rho q_{vT}^2}{D} + \Delta p_v. \end{aligned} \quad (2.3.18)$$

This also gives,

$$\Delta p_v = \frac{2\Delta U_v}{\Omega D}. \quad (2.3.19)$$

If we can group  $E$  molecules such that  $\Delta U_v/\Omega = \text{Const.}$  with respect to  $x_i$ , the pressure gradient term in the Navier–Stokes equation can be written as

$$\frac{\partial p}{\partial x_i} = \frac{\partial p_v}{\partial x_i} + \frac{\partial \Delta p_v}{\partial x_i} = \frac{\partial p_v}{\partial x_i}. \quad (2.3.20)$$

That allows us to replace  $p$  to  $p_v$  in the Navier–Stokes equations, indicating that the pressure determined by all molecule motions is not necessary for calculating the macroscopic fluid distributions.

The applicability of this concept may depend on how the group of  $E$  molecules is defined, whereas the definition of grouping is very ambiguous because the selection of  $E$  does not appear in the derived relationship in Eqs. (2.3.17)–(2.3.20). The virtual particle concept being introduced is itself identical to that of LBM; however, the present explanation of the virtual particle concept gives a theoretical understanding that pressure due to internal energy within the virtual particle is neglected in the LBM.

If we select a lattice grid,  $f_i$  and  $\mathbf{c}_i$  in Eq. (2.3.9) are explicitly determined, and therefore, we obtain the following expression for  $p_v$  (please refer to Appendix A2 for the derivation).

$$p_v = \rho \frac{c^2}{3} = \frac{\rho}{3} \left( \frac{\Delta}{\Delta t} \right)^2. \quad (2.3.21)$$

This relationship is identical to the assumption that  $a = \Delta/(\sqrt{3}\Delta t)$ . Therefore, the concept of a virtual particle justifies that speed of sound  $a$ , can be an artificial parameter, determined by the grid system of a numerical simulation. However,  $a$  is not an arbitrary parameter that can be empirically determined, but is one that is fixed by the grid system. By employing Eqs. (2.1.2) and (2.3.21), we can get the final version of the Navier–Stokes equations of EMV as follows;

$$\frac{\partial \rho u_i}{\partial t} + \frac{\partial \rho u_i u_j}{\partial x_j} = -\frac{1}{3} \left( \frac{\Delta}{\Delta t} \right)^2 \frac{\partial \rho}{\partial x_i} + \frac{\partial}{\partial x_j} (\lambda \theta \delta_{ij} + \mu e_{ij}). \quad (2.3.22)$$

As a result, we can solve  $u_i$  and  $\rho$  explicitly by Eqs. (2.1.1) and (2.3.22). Therefore, we refer to this as the explicit method with virtual particle concept (EMV). The Mach number of EMV is calculated by the following equation, which becomes larger than real;

$$Ma = \frac{V}{a} = \sqrt{3} V \left( \frac{\Delta t}{\Delta} \right) \quad (2.3.23)$$

Here,  $Ma$  is the Mach number [–] and  $V$  is the fluid velocity [m/s]. The justification for introducing the virtual particle for reproducing the velocity fields of incompressible fluids is discussed in Section 3.

### 3. Application to two-dimensional cavity flow

#### 3.1 Numerical description

A two-dimensional cavity flow has been solved using the EMV, conventional CFD (based on Simplified Marker and Cell, hereafter, denoted as SMAC [18]), and LBM. Additionally, the results were compared with reference data by Ghia et al. [19], who conducted direct numerical simulation based on coupled strongly implicit multigrid (CSI-MG) method [20]. This section describes the basic numerical conditions employed in these simulations.

Fig.1 and Table 1 show the schematic diagram of cavity and numerical conditions for each case. We consider a simple two-dimensional cavity flow in which the side and bottom walls are fixed and the top is specified as fixed velocity of  $u_t = 1\text{m/s}$ .  $\mu$  is fixed as well, and the width and height of the cavity denoted as  $H$  is determined by the Reynolds number  $Re = \rho_o u_t H / \mu$ , where  $\rho_o$  is the initial air density since  $\rho$  changes with time in EMV and LBM. Three conditions of  $Re$  number are employed:  $Re = 100$ ,  $1000$ , and  $10000$ . Grid numbers of  $100^2$ ,  $150^2$ , and  $250^2$  are used, respectively, for each  $Re$ . A uniform grid resolution  $\Delta x = \Delta y = \Delta$  is applied in  $x$  and  $y$  directions for EMV, SMAC, and LBM.

The governing equations are discretized in a staggered grid system [21] for EMV and SMAC. As for the temporal development, the first-order Euler scheme is adopted with  $\Delta t = C_o \Delta / u_t$  for SAMC and  $\Delta t = C_o \Delta / (u_t + a)$  for EMV and LBM. Here,  $C_o$  is the Courant number. For SMAC method,  $C_o = 0.25$ , whereas  $C_o = u_t \Delta t / \Delta + 1/\sqrt{3} \sim 0.83$  for EMV and LBM in the present simulations. We employed the different Courant numbers in SMAC and other methods because we employed the same  $\Delta t$  for all the simulations. The advection, diffusion, and pressure terms are discretized by the second-order central scheme, whereas the first-order upwind and total variation diminishing (TVD) scheme [22] are employed for advection terms of continuity and Navier–Stokes equations when  $Re = 10000$ . This is because the numerical oscillations cannot be reduced in the EMV with  $Re = 10000$ . It should be noted that we were able to obtain the converged flow fields even though the second-order central scheme was employed in the advection term in the explicit methods of SMAC and EMV due to the molecular and numerical diffusion terms. The details of discretization are given in Appendix A2. LBM employs a 2D9V (two-dimensional and nine-discrete particle speeds) grid system with the BKG model [23] with collocation grids.

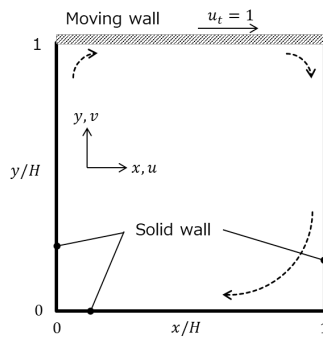


Fig.1 Schematic diagram of numerical domain.

Table 1. Numerical settings for compared simulations and reference data.

Method	Variables to be solved	Storage	Discretization	
			Advection	Diffusion/Gradient
EMV ( $Re = 100, 1000$ )	$u_i, \rho$	1 <sup>st</sup> - Euler	2 <sup>nd</sup> - central	2 <sup>nd</sup> - central
EMV ( $Re = 10000$ )	$u_i, \rho$	1 <sup>st</sup> - Euler	1 <sup>st</sup> -upwind ( $\rho$ ) TVD ( $u_i$ )	2 <sup>nd</sup> - central



SMAC	$u_i, p$	1 <sup>st</sup> - Euler	2 <sup>nd</sup> - central	2 <sup>nd</sup> - central
LBM	$f_i$	-	-	-
Ghia et al. [19]	$u_i, p$	-	Khosla et al. [24]	2 <sup>nd</sup> - central

### 3.2 Converged flow distribution

Fig. 2 shows snapshots of the streamlines and  $p$  distribution at  $t = t_e$  for each  $Re$  number. Here,  $t_e$  represents the time when flow fields converge.  $p$  in EMV and LBM represent the values determined by  $\rho$  from distribution of Eq. (2.3.21). As can be seen in Fig. 2 (a–c) of  $Re = 100$ , three calculation methods show identical primary vortex as well as pressure distribution in a steady-state condition. Additionally, the secondary vortices shown at both bottom corners are also well captured for all three methods. When  $Re = 1000$  in Fig. 2 (d–f), similar results can be seen; i.e., both primary and secondary vortices were well reproduced for each method. In the case of  $Re = 10000$ , the EMV in Fig. 2 (g) reproduces the primary vortex and vortices in the bottom-right corner as those in SMAC in Fig. 2 (h). Additionally, subsidiary vortices in the bottom-right and left-top corners are seemingly identical. In contrast, slight differences in the vortex shapes near the left-bottom corner can be observed. Although the LBM can capture the primary vortex consistent with the other two methods, the shapes of subsidiary vortices differ from those of EMV or SMAC. This result means that both the EMV and LBM employed identical concepts for determining  $p$ ; however, the reproduced flow field slightly differed from each other. In contrast, EMV and SMAC show significantly similar flow patterns regardless of the difference in the governing equations.

Regarding numerical stability for each simulation, a slight numerical oscillation can be seen at pressure distribution of  $Re = 10000$  near the right wall ( $x/H \sim 0.9, y/H \sim 0.5$ ) only in EMV (Fig. 2 (g)), although both SMAC (Fig. 2 (h)) and LBM (Fig. 2 (i)) do not show any unnatural fluctuations. This is confirmed by exploring time evolutions of  $u$  and  $p$  at several points, despite not showed in this paper. The dominant frequency of these oscillations in EMV are much higher frequency than the frequency of propagations of the sound waves. Thus, we concluded that this oscillation is because EMV solves the governing equations explicitly, whereas SMAC employs iterative simulation by solving the Poisson equation of  $p$ .

The velocity profiles of the EMV are compared with those of SMAC, LBM, and direct numerical simulation (DNS) results (Ghia et al. (1982) [19]) in Fig. 3. The vertical profiles of  $u$  and horizontal profiles of  $v$  are taken at  $x/H=0.5$  and  $y/H=0.5$ , respectively. Both velocity components are normalized by  $u_t$ . As can be seen in Figs. 3 (a) and (b), the results of EMV show profiles identical to those of SMAC and Ghia et al. (1982) at  $Re = 100$  and 1000, indicating that EMV can reproduce the flow fields, similar to the conventional method, even though explicit numerical method is employed.

On the other hand, the profile of EMV is underestimated by approximately 15% at maximum as compared with those of SMAC and DNS,  $Re = 10000$  as shown in Fig. 3 (c). The difference is the most significant at the peaks of  $u$  and  $v$  near each wall. Furthermore, a slight numerical oscillation of  $v$  can be admitted between  $x/H=0.9$  and 1.0. Both of these aspects are due to the difference in the spatial discretization scheme between EMV and SMAC, i.e., SMAC employed the second-order central scheme for the advection term, whereas EMV inevitably adopted the first-order upwind scheme for the advection term in  $\rho$  equation and TVD scheme in  $u_i$  equations. This means that the artificial numerical viscosity was added only in the EMV to avoid numerical oscillation, which led to deviations between EMV and SMAC. As shown in Appendix A3, we confirmed that 2-D cavity flows using the first-order upwind deference scheme for both EMV and SMAC does not show any differences in velocity distributions, although the results are different from DNS data (Ghia 1982). These

results imply that EMV can reproduce the velocity fields similar to those in conventional methods wherein the perfect incompressibility of fluid is assumed, although we have to employ an appropriate advection scheme to avoid numerical oscillation and obtain converged flow fields.

In contrast to these slight differences in EMV and SMAC, LBM shows larger differences in both  $u$  and  $v$ . It should be noted that the discrepancies of EMV from SMAC and DNS are much smaller than those of LBM, especially at  $Re = 10000$ .

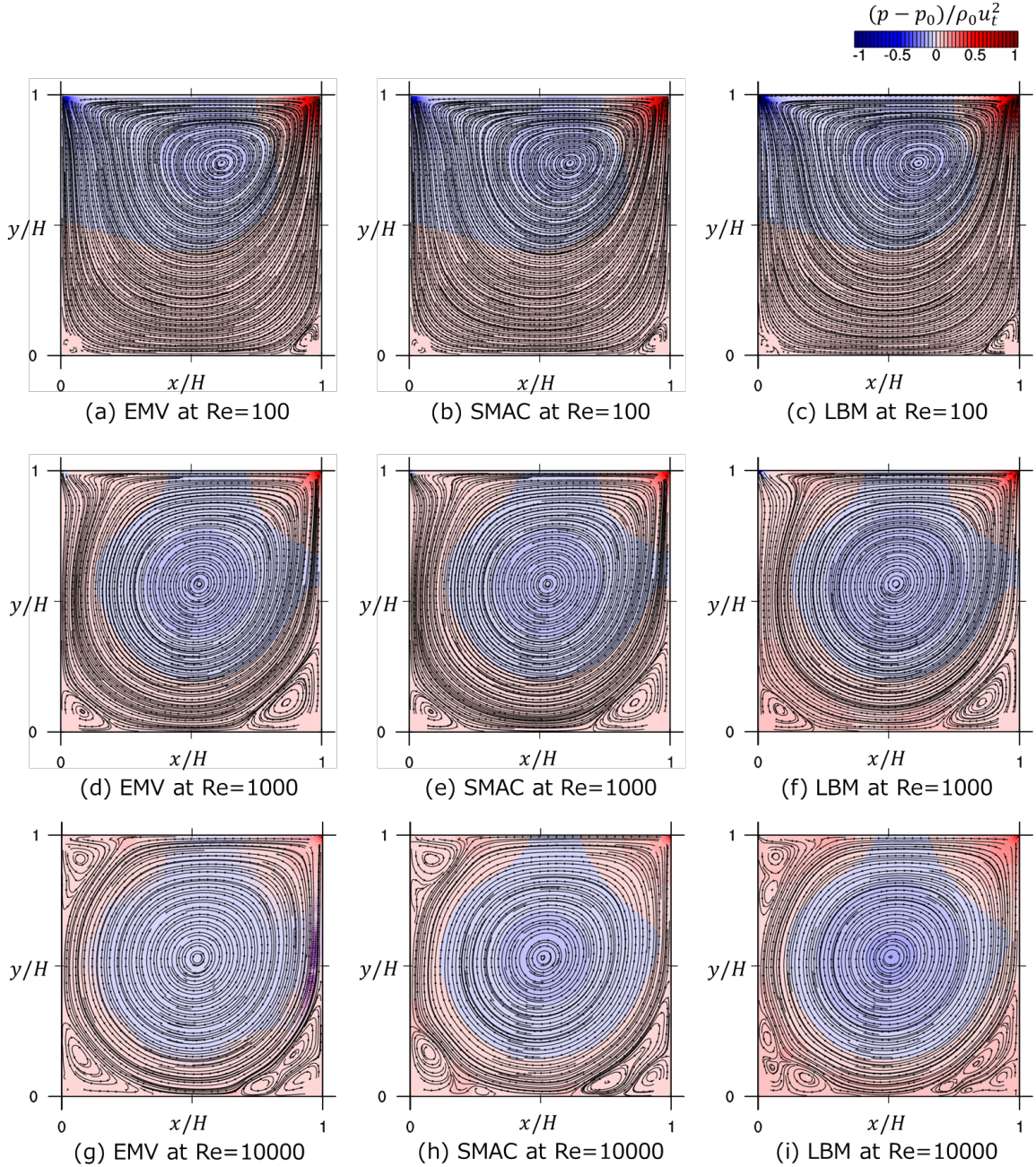
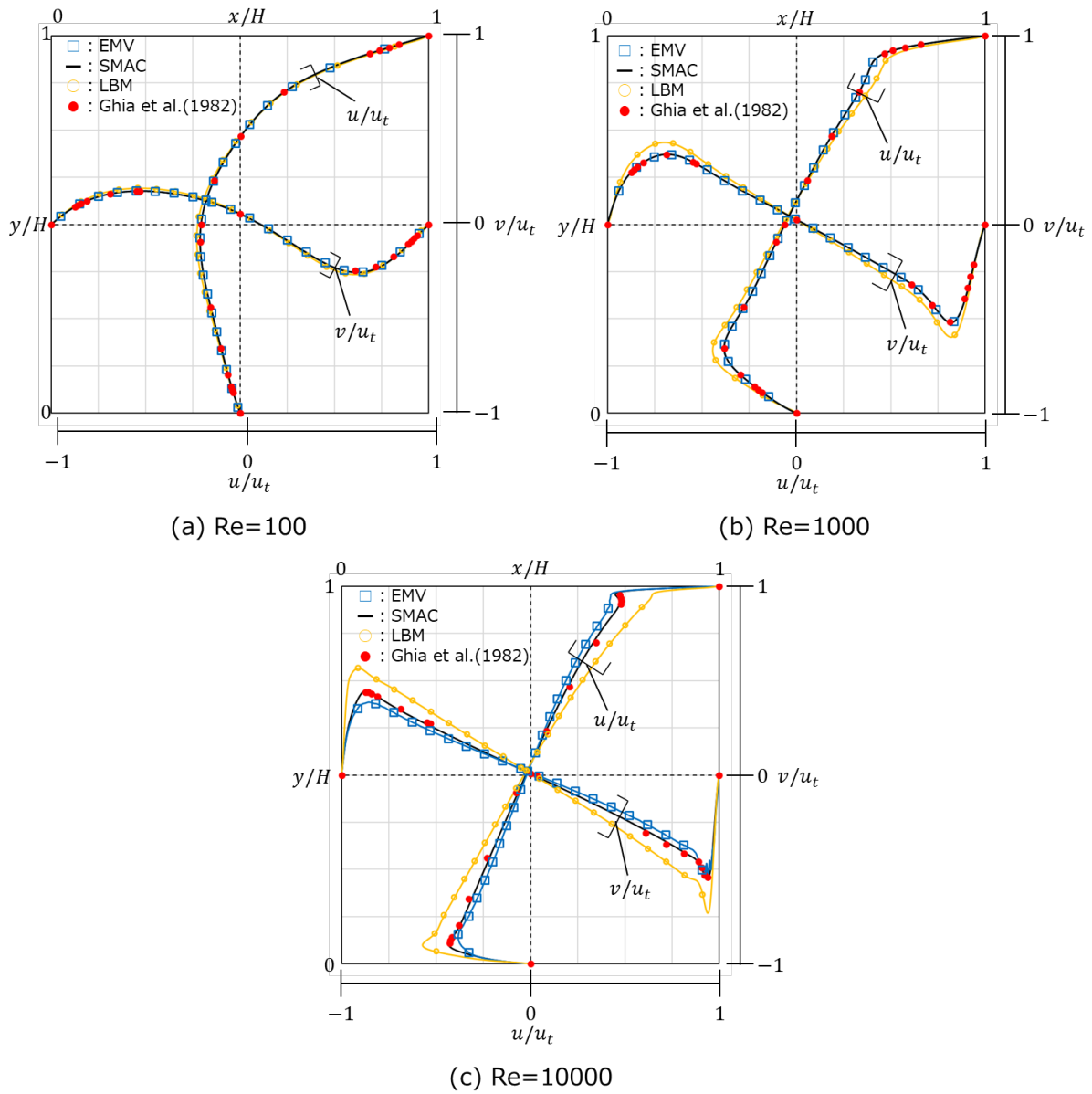


Fig.2 Streamlines and pressure distributions at each Reynolds number of (a-c)  $Re = 100$ , (d-f)  $Re = 1000$ , and (g-i)  $Re=10000$  at time,  $t/t_e = 1$ , where  $t_e$  is the duration when the flow distribution converges.  $p_0$  is the initial pressure value. The distributions are determined by (a), (d), (c) EMV, (b), (e), (h) SMAC, and (c), (f), (i) LBM.



385

386 Fig.3 Velocity profiles in the center line of cavity for  $u$  at  $x/H = 0.5$  and  $v$  at  $y/H =$   
 387  $0.5$ . (a)  $Re = 100$ , (b)  $Re = 1000$ , and (c)  $Re = 10000$ . Reference data is after Ghia et al.  
 388 (1982).

### 3.3. Temporal evolutions

The other concern is whether EMV can reproduce the temporal evolutions of the velocity fields consistent with the conventional method. In this section, we qualitatively discuss the temporal development of flow by comparing changes in the vortex structures within the cavity, and time evolutions of velocity at the center of the cavity.

Fig.4 shows the flow distributions determined by EMV and SMAC,  $Re = 1000$  at three different moments of  $t/t_e = 0.05$ ,  $0.2$ , and  $0.4$  (The distributions at  $Re = 100$  does not show significant difference between EMV and SMAC; therefore, we discuss the patterns of  $Re = 1000$  and  $10000$ ).  $t/t_e = 0.05$  in Figs. 4 (a) and (d), we can see the difference in streamlines at the bottom of the cavity, although the overall distribution patterns are similar to each other in terms of streamlines and locations of the primary vortex near  $x/H = y/H \sim 0.8$ . Additionally, the  $p$  distribution seems to show some difference. Such a difference may be due to the effect of acoustic wave propagating with the speed of sound. In SMAC, the assumption of incompressibility indicates that the propagating speed of acoustic wave is infinite, which is enabled by solving the Poisson equation of  $p$ . In contrast, the propagating speed in EMV is the artificial speed of sound  $a = \Delta/\sqrt{3}\Delta t$  by solving the compressible continuity equation as explained in Section 2.3. Such differences become less significant as the time step evolves, as shown in Figs.4 (b) and (e), and Figs. 4 (c) and (f). At  $t/t_e = 0.2$ , the streamline and pressure distribution show good agreement except for the secondary vortex in the bottom-right corner of the cavity. Accordingly, the difference in flow patterns cannot be seen at  $t/t_e = 0.4$ .

Fig. 5 looks the same as Fig. 4 but for  $Re = 10000$ .  $t/t_e = 0.03$  in Figs. 5 (a) and (d), both results have two vortices near the center of the cavity; however, the shapes and locations of the two vortices differ in EMV and SMAC. Additionally, the secondary vortices observed near three corners of the cavity (i.e.,  $(x/H, y/H) \sim (0.1, 0.1)$ ,  $(0.1, 0.9)$ , and  $(0.9, 0.1)$ ) show significant differences. For example, at  $(0.1, 0.1)$ , the core of the vortex is located at a lower and righter position for EMV than SMAC. With time development, these two vortices near the cavity center combine with each other and one primary vortex is formed at the center of the cavity, as seen in Figs. 5 (b) and (e). At this moment, the flow distributions are considerably similar in EMV and SMAC; however, slight differences can be observed near each corner. At  $t/t_e = 0.2$  in Figs. 5 (c) and (f), the results of both EMV and SMAC are almost identical, although the numerical oscillations occur near the side wall, as seen in the profiles of  $v$  (in Fig. 3. (c)).

Figs. 6 and 7 show the temporal evolutions of  $u$ ,  $v$ , and  $p$  at the center of the cavity ( $x/H = 0.5$ ,  $y/H = 0.5$ ), and the maximum and minimum density,  $\rho_{max}$  and  $\rho_{min}$ , within the entire domain at each time step to qualitatively discuss the differences in each method. The horizontal axis is normalized by  $t_e$ .

At  $Re = 100$ , both  $u$  and  $p$  by EMV show the apparent oscillation from  $t/t_e = 0$  to  $0.4$ , whereas those of SMAC do not fluctuate at all. Similar oscillations can be seen for the LBM. With temporal development, such oscillations decrease for EMV. Consequently,  $u$ ,  $v$ , and  $p$  of the EMV agree well with those of the SMAC. These differences among the methods mean that the explicit method causes such oscillations with respect to time. However, we could not differentiate these oscillations from the numerical oscillation because they can occur due to the propagation of a wave with finite speed of sound. Additionally, we have to assume that the considerable smooth temporal development of velocity and  $p$  is unnatural owing to the iterative method while solving the Poisson equation of  $p$  in SMAC. Note that the difference in approached values of  $t = t_e$  among EMV, SMAC, and LBM reflects the differences shown in profiles of Fig. 3. A similar trend can be seen when  $Re = 1000$  in Figs.



6 (c) and (d). Regarding the compressible effect in EMV, Fig. 7 shows that the maximum difference in the density is less than  $\pm 5\%$ .

Alternatively, Figs. 3 (e) and (f),  $Re = 10000$  show that oscillations of  $u$ ,  $v$ , and  $p$  of EMV are not reduced even though time evolves. In contrast, those of SMAC show significantly smooth changes with time. We cannot state that these fluctuations are artificial or numerical problems; however, such fluctuations may cause the divergence of numerical simulation and must be avoided for the numerically stable simulations. In addition, such oscillations can also be seen in  $\rho_{max}$  and  $\rho_{min}$  of EMV (Fig. 7). However, the difference of the density within the entire domain is kept less than 8% at  $Re = 10000$ .

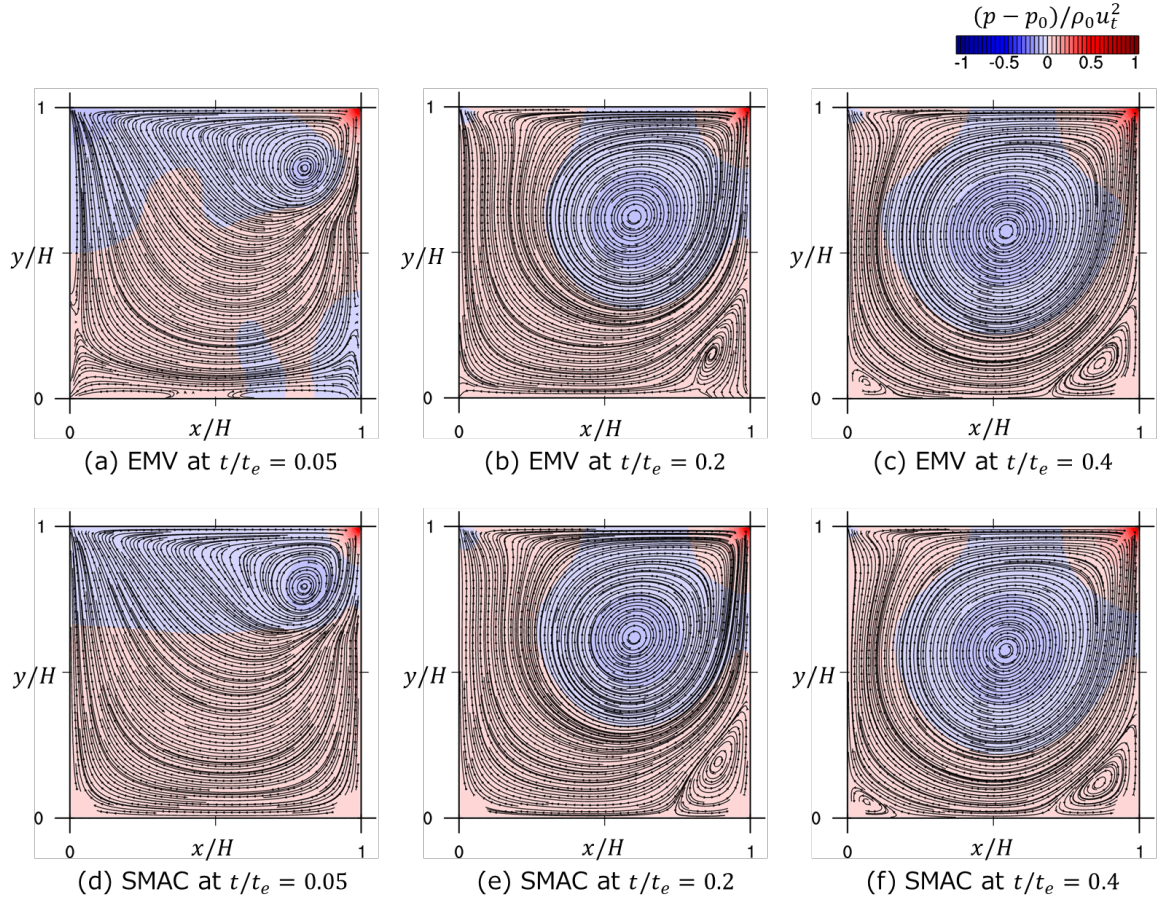


Fig.4 Temporal changes in velocity distributions for  $Re = 1000$  for (a–c) EMV and (d–f) SMAC. (a), (d) at  $t/t_e = 0.05$ , (b), (e),  $t/t_e = 0.2$  and (c), (f)  $t/t_e = 0.4$ .

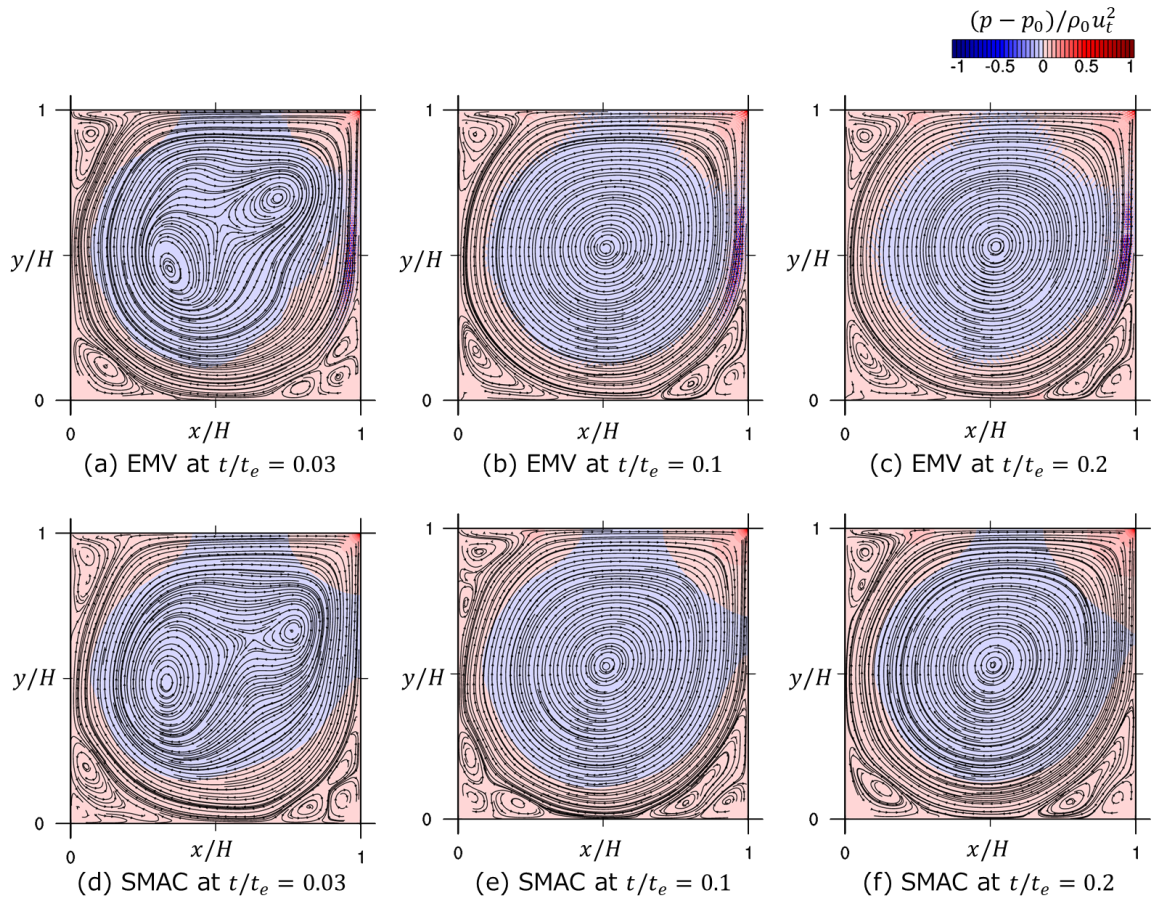


Fig.5 Same as Fig. 4, but for  $Re = 10000$ . (a) (d) at  $t/t_e = 0.03$ , (b), (e),  $t/t_e = 0.1$  and (c), (f)  $t/t_e = 0.2$ .

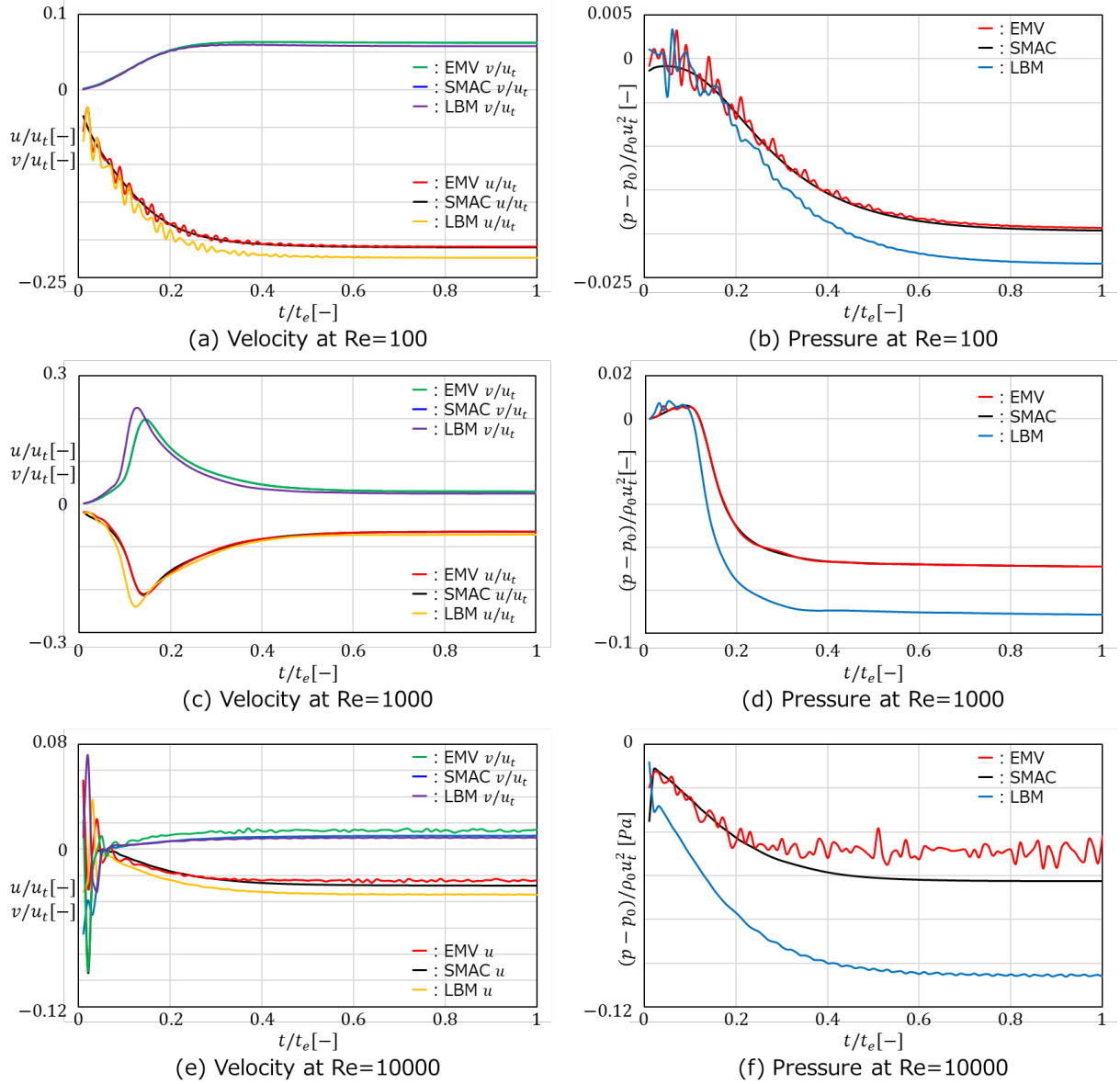


Fig.6 Temporal evolutions of velocity and pressure at center of cavity ( $x/H = 0.5$  and  $y/H = 0.5$ ) for (a,b)  $Re = 100$ , (c,d)  $Re = 1000$ , and (e,f)  $Re = 10000$ .

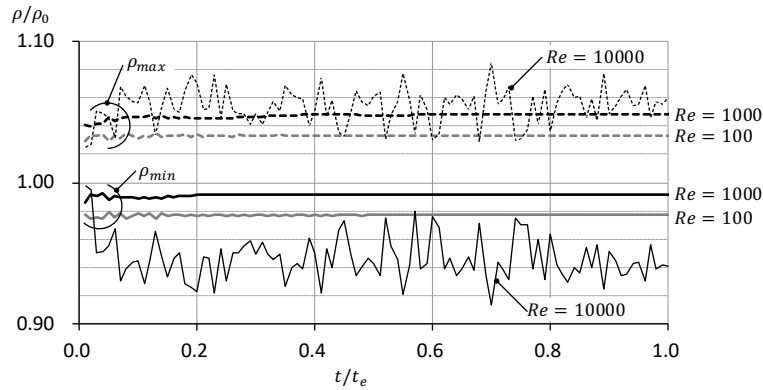


Fig. 7 Temporal evolutions of maximum and minimum density,  $\rho_{max}$  and  $\rho_{min}$  within the entire domain at each time step.  $\rho_0$  indicates the density at the initial condition.

#### 4. Conclusion

In this paper, we discussed the theoretical interpretation of an artificially compressible method such as ACM and EDACM to propose a new explicit numerical method for numerical simulation of fluid flow. The new method, the explicit numerical method with virtual particle concept called as EMV, employs the compressible continuity and Navier–Stokes equations by replacing the pressure to density with an artificial parameter. Additionally, the validity of EMV was proven by comparing the results of the two-dimensional cavity flow among the conventional and reference numerical simulations.

In theoretical derivation, we confirmed that ACM and EDACM correspond to barotropic and isochoric conditions, respectively, by comparing the set of equations employed in ACM and EDACM with theoretically derived equations for the three macroscopic states. Previous studies have stated that ACM corresponds to the isentropic state; however, we extended the interpretation of ACM as a barotropic condition including both isothermal and isentropic states. Additionally, we provided a new interpretation of EDACM as the isochoric conditions. Moreover, we clarified the potential problems in artificial compressibility method: i) both ACM and EDACM may violate the mass conservation law under unsteady-state conditions, and ii) the governing equations of both methods cannot explain why artificial compressibility method can be employed with  $\alpha$  as an arbitrary model parameter.

To overcome these problems, we propose a new simulation method called EMV, which employs compressible continuity and Navier–Stokes equations. By introducing the virtual particle concept, we provide a theoretical interpretation of replacing  $\alpha$  as an artificial parameter determined by the grid system of numerical simulation.

To confirm the validity of EMV, a numerical simulation of two-dimensional cavity flow was compared with EMV, SMAC, LBM, and previous numerical simulations for three conditions of  $Re = 100$ ,  $1000$ , and  $10000$ . The results of EMV agree well with SMAC and reference data for both steady-state and temporal evolutions in comparison with those of LBM at  $Re = 100$  and  $1000$ . In contrast, when  $Re = 10000$ , the numerical oscillation could be seen only in the EMV results. Hence we conclude that such oscillations are due to the numerical instability of the advection term, which can be avoided by applying a numerically suitable scheme even in EMV.

Although the proposed method was verified in terms of theoretical framework with the virtual particle concept as well as numerical feasibility, comparable with previous methods, our numerical simulations employed in this study were very simple for two-dimensional cavity flow. Furthermore, we only employed the staggered grid system by using SMAC and EMV methods. The proposed method will be adopted for various flows with difference grid systems in future studies, yielding the development of an explicit method for numerically efficient simulation.

#### Acknowledgments

This study was partially supported by a Grant-in-Aid for Scientific Research from JSPS, Japan, KAKENHI (Grant No. JP17H04946, JP17KK0117, and JP 20H02314). We would like to express our gratitude to them. We would like to thank Editage ([www.editage.com](http://www.editage.com)) for English language editing.



## Appendix

### A1. Distribution function of a virtual particle

The distribution function of molecules is expressed by the Maxwell distribution as follows:

$$f(\mathbf{q}) = \left(\frac{m\beta}{2\pi}\right)^{\frac{3}{2}} \exp\left(-\frac{m\beta}{2}\mathbf{q}^2\right). \quad (\text{A1.1})$$

Here,  $\mathbf{q}$  and  $m$  represent the velocity and mass of molecules,  $\beta = 1/k_B T$  is the inverse temperature, and  $k_B$  is the Boltzmann constant. When all the molecules are exposed to a macroscopic velocity  $\mathbf{u}$ , the distribution is modified as

$$f(\mathbf{q}) = \left(\frac{m\beta}{2\pi}\right)^{\frac{3}{2}} \exp\left(-\frac{m\beta}{2}(\mathbf{q} - \mathbf{u})^2\right), \quad (\text{A1.2})$$

because the relative velocity of molecules becomes  $\mathbf{q} - \mathbf{u}$ .

We assume that the distribution function of virtual particles,  $f_i$ , can be expressed by a similar function by applying the Taylor series expansion up to  $\mathbf{u}^2$ :

$$f_i = A_i[1 + B\mathbf{u} \cdot \mathbf{u} - 2B\mathbf{c}_i \cdot \mathbf{u} + 2B^2(\mathbf{c}_i \cdot \mathbf{u})^2]. \quad (\text{A1.3})$$

Here,  $A_i$  ( $i = 0$  to  $M$ , where  $M$  is the number of velocities in a lattice grid) and  $B = -3/2c^2$  ( $c = \Delta/\Delta t$ , where  $\Delta$  is the representative speed of virtual particles defined by the shortest grid length and the representative time scale  $\Delta t$ ) are determined to satisfy the macroscopic nature of a fluid, independently. The ultra-discretized velocity is denoted as  $\mathbf{c}_i$  ( $i = 0$  to  $M$ ).  $A_i$  and  $\mathbf{c}_i$  are determined once a lattice grid on which the virtual particles can move is selected. If we employ the typical velocity and lattice grid models used in the Lattice-Boltzmann method, as shown in Fig. A1, we can obtain these coefficients, as listed in Table A1.

By using these coefficients,  $q_{vT}$  is explicitly determined as

$$q_{vT} = \sum_i f_i \mathbf{c}_i^2 = \frac{D}{3} c^2, \quad (\text{A1.4})$$

regardless of the selection of the lattice grid. This also gives the simplest form of  $p_v$  as

$$p_v = \rho \frac{c^2}{3} = \frac{\rho}{3} \left(\frac{\Delta}{\Delta t}\right)^2. \quad (\text{A1.5})$$

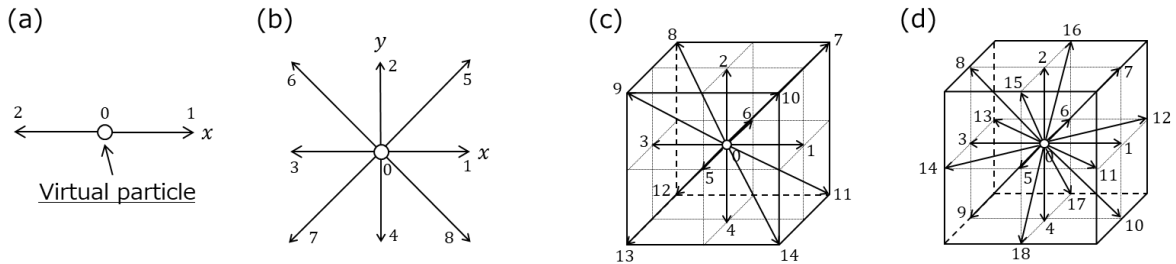


Fig. A1 Definition of lattice grids (a) 1D3V, (b) 2D9V, (c) 3D15V, and (d) 3D19V models

Table A1: Coefficient for the discrete distribution function  $f_i$ . For 1D3V,  $C_1 = A_0$  and  $C_2 = A_1 = A_2$ , for 2D9V,  $C_1 = A_0$ ,  $C_2 = A_1$  to  $A_4$ , and  $C_3 = A_5$  to  $A_8$ , for 3D15,  $C_1 = A_0$ ,  $C_2 = A_1$  to  $A_6$ , and  $C_3 = A_7$  to  $A_{14}$ , and for 3D19V,  $C_1 = A_0$ ,  $C_2 = A_1$  to  $A_6$ , and  $C_3 = A_7$  to  $A_{18}$ .

Lattice grid types	$C_1$	$C_2$	$C_3$
1D3V	2/3	1/6	-
2D9V	4/9	1/9	1/36
3D15V	2/9	1/9	1/72
3D19V	1/3	1/18	1/36

## A2. Discretization

For two-dimensional cavity flow of compressible fluids, the governing equations with virtual particle concepts can be written as follows:

$$\frac{\partial \rho}{\partial t} + \frac{\partial \rho u}{\partial x} + \frac{\partial \rho v}{\partial y} = 0, \quad (\text{A2.1})$$

$$\frac{\partial \rho u}{\partial t} + \frac{\partial \rho u^2}{\partial x} + \frac{\partial \rho uv}{\partial y} = -\frac{c^2}{3} \frac{\partial \rho}{\partial x} + \mu \frac{\partial^2 u}{\partial x^2} + \mu \frac{\partial^2 u}{\partial y^2}, \quad (\text{A2.2})$$

$$\frac{\partial \rho v}{\partial t} + \frac{\partial \rho uv}{\partial x} + \frac{\partial \rho v^2}{\partial y} = -\frac{c^2}{3} \frac{\partial \rho}{\partial y} + \mu \frac{\partial^2 v}{\partial x^2} + \mu \frac{\partial^2 v}{\partial y^2}. \quad (\text{A2.3})$$

By replacing the pressure term with  $\rho$  and  $c = \Delta/\Delta t$  based on the virtual particle concept, the first equation obtained is the continuity, and the latter two are Navier–Stokes (NS) equations. The second viscosity terms in NS equations do not appear in two-dimensional cases because  $\lambda = -\mu$ . The variables are defined at each stencil based on staggered grids. The velocity  $u$ ,  $v$ , and density  $\rho$  are defined at  $(i, J)$ ,  $(I, j)$  and  $(I, J)$  as shown in Fig. A1. These variables are denoted as,  $u_{ij}$ ,  $v_{Ij}$ , and  $\rho_{IJ}$ . When a quantity that is not defined at the grids is required, the values are interpolated by variables defined on the grids. The interpolation method is explained in each budget equation.

The discrete form of continuity is derived by following the finite volume method as

$$\int_{V_{IJ}} \frac{\partial \rho}{\partial t} dV + \int_{V_{IJ}} \left( \frac{\partial \rho u}{\partial x} + \frac{\partial \rho v}{\partial y} \right) dV = 0. \quad (\text{A2.4})$$

By taking the average volume with respect to the cell  $V_{IJ}$  for  $\rho_P = \rho_{IJ}$  (Fig. A2), where the subscript  $P$  indicates the present position when volume is considered. By employing the first-order Euler discretization method for storage term and defining the numerical flux at the boundary  $b$  ( $=e, w, s, \text{ and } n$ ),  $\phi_b^*$ , Eq. (A2.4) is written as

$$\rho_{IJ}^{n+1} = \rho_P - \frac{\Delta}{a_0} (\phi_e^* u_e - \phi_w^* u_w + \phi_n^* v_n - \phi_s^* v_s), \quad (\text{A2.5})$$

where,  $u_e = u_{i+1, J}$ ,  $u_w = u_{i, J}$ ,  $v_n = v_{I, j+1}$ ,  $v_s = v_{I, j}$ , and  $a_0 = \Delta^2/\Delta t$ . The superscript  $n+1$  represents the value at time step  $n+1$ . The variables without the superscript indicate the value at the time step of  $n$ .  $\phi_b^*$  is defined as a general numerical flux form by employing a parameter  $\psi$  as

$$\phi_b^* = \phi_U + 0.5\psi(\phi_D - \phi_U). \quad (\text{A2.6})$$

Here, the subscripts  $U$  and  $D$  indicate the quantities at the upwind and downwind stencils with respect to  $b$  in Fig. A1 (b).  $\phi_b^*$  can be written in a form consistent with the central interpolation schemes as

$$\phi_b^* = 0.5(\phi_U + \phi_D) + 0.5(1 - \psi)(\phi_U - \phi_D). \quad (\text{A2.7})$$

$\psi$  can be used to control the numerical viscosity to avoid numerical oscillation.  $\psi = 0$  and  $\psi = 1$  correspond to upwind and central interpolation schemes, respectively. The total variation diminishing (TVD) scheme requires  $\psi$  to be in TVD region as a function of the local gradient  $r_b$ . An example of  $\psi(r_b)$  is the van Albada limiter function [22], as used in this paper.

$$\psi(r_b) = \frac{r_b + r_b^2}{1 + r_b^2}, \quad (\text{A2.8})$$

$$r_b = \frac{\phi_U - \phi_{UU}}{\phi_D - \phi_U}. \quad (\text{A2.9})$$

Here, the superscript  $UU$  indicates the two-grid upwind stencil with respect to  $b$  in Fig. A2(b).

By substituting Eq. (A2.7) in Eq. (A2.5), the discrete continuity equation can be written as the form consistent with the central interpolated scheme as

$$\rho_{i,j}^{n+1} = \left(1 + \frac{a_P - b_P}{a_O}\right) \rho_P + \Sigma_M \frac{a_M + b_M}{a_O} \rho_M. \quad (\text{A2.10})$$

Here, the coefficients are defined as follows:  $a_E = -0.5u_e\Delta$ ,  $a_W = 0.5u_w\Delta$ ,  $a_N = -0.5v_n\Delta$ ,  $a_S = 0.5v_s\Delta$ ,  $b_E = 0.5(1 - \psi(r_e))|u_e|\Delta$ ,  $b_W = 0.5(1 - \psi(r_w))|u_w|\Delta$ ,  $b_N = 0.5(1 - \psi(r_n))|v_n|\Delta$ ,  $b_S = 0.5(1 - \psi(r_s))|v_s|\Delta$ ,  $a_P = \Sigma_M a_M$  and  $b_P = \Sigma_M b_M$ .  $\Sigma_M$  means taking all summation with respect to the surrounding stencils of  $M = E, W, N$  and  $S$  (Fig. A2 (b)).

Similarly, the momentum equation of  $u$  can be integrated with respect to the volume  $V_{i,j}$  for  $u_P = u_{i,j}$  as

$$\int_{V_{i,j}} \frac{\partial \rho u}{\partial t} dV + \int_{V_{i,j}} \left( \frac{\partial \rho u^2}{\partial x} + \frac{\partial \rho uv}{\partial y} \right) dV = -\frac{c^2}{3} \int_{V_{i,j}} \frac{\partial \rho}{\partial x} dV + \int_{V_{i,j}} \left( \mu \frac{\partial^2 u}{\partial x^2} + \mu \frac{\partial^2 u}{\partial y^2} \right) dV. \quad (\text{A2.11})$$

By employing the first-order Euler scheme for storage, the central interpolation scheme for diffusion terms, and the numerical flux in the advection terms, the discrete form can be written as follows:

$$u_P^{n+1} = \left( \frac{\rho_P}{\rho_P^{n+1}} - \frac{c_P}{c_O \rho_P^{n+1}} \right) u_P - \frac{c^2 \Delta}{3 c_O \rho_P^{n+1}} (\rho_e^{n+1} - \rho_w^{n+1}) + \frac{1}{c_O \rho_P^{n+1}} \Sigma_M c_M u_M + \frac{\Delta}{c_O \rho_P^{n+1}} (\rho_e \phi_e^* - \rho_w \phi_w^* + v_n \phi_n^* - v_s \phi_s^*). \quad (\text{A2.12})$$

Here,  $\rho_e = \rho_{i,j}$ ,  $\rho_w = \rho_{i-1,j}$ ,  $\rho_e^{n+1} = \rho_{i,j}^{n+1}$ ,  $\rho_w^{n+1} = \rho_{i-1,j}^{n+1}$ ,  $\rho_P = 0.5(\rho_e + \rho_w)$ ,  $\rho_P^{n+1} = 0.5(\rho_e^{n+1} + \rho_w^{n+1})$ ,  $v_n = 0.5(v_{i,j+1} + v_{i-1,j+1})$ ,  $v_s = 0.5(v_{i,j} + v_{i-1,j})$ . The coefficients are defined as follows:  $c_O = \Delta t / \Delta^2$ ,  $c_E = c_W = c_N = c_S = \mu$ ,  $c_P = \Sigma_M c_M$ .  $\phi_e^*$  and  $\phi_w^*$ , and,  $\phi_n^*$  and  $\phi_s^*$ , are determined by taking  $\phi = u^2$  and  $\phi = \rho u$  in Eq. (A2.6), respectively.  $\rho_P^{n+1}$  is taken at  $n+1$  time step, for consistency of the discrete form for  $\partial \rho u / \partial t$  and  $u \partial \rho / \partial t + \rho \partial u / \partial t$ . Moreover, the densities in term  $\partial \rho / \partial x$  are determined by the values at  $n+1$  time step using Eq. (A2.10), which is solved before the momentum equations because of the convergence of Eq. (A2.12).

In the same matter, the momentum equation of  $v$  can be integrated with respect to the volume  $V_{i,j}$ , and the following equation can be obtained.

$$v_P^{n+1} = \left( \frac{\rho_P}{\rho_P^{n+1}} - \frac{d_P}{d_O \rho_P^{n+1}} \right) v_P - \frac{c^2 \Delta}{3 d_O \rho_P^{n+1}} (\rho_n^{n+1} - \rho_s^{n+1}) + \frac{1}{d_O \rho_P^{n+1}} \Sigma_M d_M v_M + \frac{\Delta}{d_O \rho_P^{n+1}} (u_e \phi_e^* - u_w \phi_w^* + \rho_n \phi_n^* - \rho_s \phi_s^*). \quad (\text{A2.13})$$

Here,  $\rho_n = \rho_{i,j}$ ,  $\rho_s = \rho_{i,j-1}$ ,  $\rho_n^{n+1} = \rho_{i,j}^{n+1}$ ,  $\rho_s^{n+1} = \rho_{i,j-1}^{n+1}$ ,  $\rho_P = 0.5(\rho_n + \rho_s)$ ,  $\rho_P^{n+1} = 0.5(\rho_n^{n+1} + \rho_s^{n+1})$ ,  $u_e = 0.5(u_{i+1,j} + u_{i,j+1})$ ,  $u_w = 0.5(u_{i,j} + u_{i,j-1})$ . The coefficients are defined as follows:  $d_O = \Delta t / \Delta^2$ ,  $d_E = d_W = d_N = d_S = \mu$ ,  $d_P = \Sigma_M d_M$ .  $\phi_e^*$  and  $\phi_w^*$ , and,  $\phi_n^*$  and  $\phi_s^*$ , are determined by taking  $\phi = \rho v$  and  $\phi = v^2$  in Eq. (A2.6), respectively.

When the numerical flux at boundary  $b$  can be estimated by each interpolated value at  $b$ , Eqs. (A2.12) and (A2.13) can be written in a form consistent with the central interpolated schemes as follows:

$$u_P^{n+1} = \left( \frac{\rho_P}{\rho_P^{n+1}} + \frac{f_P - c_P - g_P}{c_O \rho_P^{n+1}} \right) u_P - \frac{c^2 \Delta}{3 c_O \rho_P^{n+1}} (\rho_e^{n+1} - \rho_w^{n+1}) + \Sigma_M \frac{c_M + 0.5 f_M + g_M}{c_O \rho_P^{n+1}} u_M, \quad (\text{A2.14})$$

$$v_P^{n+1} = \left( \frac{\rho_P}{\rho_P^{n+1}} + \frac{h_P - d_P - k_P}{d_O \rho_P^{n+1}} \right) v_P - \frac{c^2 \Delta}{3 d_O \rho_P^{n+1}} (\rho_n^{n+1} - \rho_s^{n+1}) + \Sigma_M \frac{d_M + 0.5 h_M + k_M}{d_O \rho_P^{n+1}} v_M. \quad (\text{A2.15})$$

Here, the additional coefficients are defined as follows:  $f_E = -\rho_e \phi_e^* \Delta$ ,  $f_W = \rho_w \phi_w^* \Delta$ ,  $f_N = -v_n \phi_e^* \Delta$ ,  $f_S = v_s \phi_s^* \Delta$ ,  $f_P = \Sigma_M f_M$ .  $\phi_e^*$  and  $\phi_w^*$  are interpolated values using Eq. (A2.6) with  $\phi = u$ , and  $\phi_n^*$  and  $\phi_s^*$  are interpolated values using Eq. (A2.6) with  $\phi = \rho$ .  $g_B = 0.5|f_B|(1 - \psi(r_b))$  for  $B = E, W, N$  and  $S$ ,  $g_P = \Sigma_M g_M$ . Similarly,  $h_E = -u_e \phi_e^* \Delta$ ,  $h_W = u_w \phi_w^* \Delta$ ,  $h_N = -\rho_n \phi_e^* \Delta$ ,  $h_S = \rho_s \phi_s^* \Delta$ ,  $h_P = \Sigma_M h_M$ .  $\phi_e^*$  and  $\phi_w^*$  are interpolated

values by Eq. (A2.6) with  $\phi = \rho$ , and  $\phi_n^*$  and  $\phi_s^*$  are interpolated values using Eq. (A2.6) with  $\phi = v$ .  $k_B = 0.5|h_B|(1 - \psi(r_b))$  for  $= E, W, N$  and  $S$ ,  $k_P = \Sigma_M k_M$ .

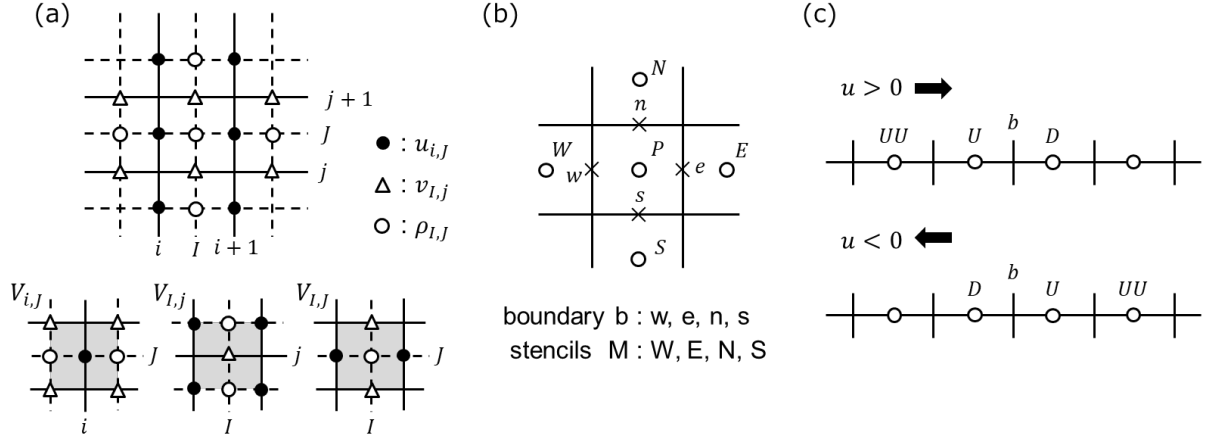


Fig.A2 Grid definition. (a) variables on the staggered grid and control volume  $V_{IJ}$ ,  $V_{ij}$ , and  $V_{Ij}$ , (b) boundary  $b$  ( $=w, e, s$ , and  $n$ ) and stencils  $M$  ( $=W, E, S$ , and  $N$ ), and (c) stencils of  $UU$ ,  $U$ , and  $D$  with respect to the boundary  $b$  for the TVD scheme.

### A.3 Comparisons between EMV and SMAC with upwind scheme

In Section 3, we clarified that EMV and SMAC showed slight differences in the velocity fields at  $Re = 10000$ . This is because of the difference in the numerical scheme for discretization of the advection term, but is not due to the proposed method where  $a = \Delta/\sqrt{3}\Delta t$ . To confirm this aspect, the results are presented here by applying the first-order upwind scheme in both continuity and N-S equations for EMV and SMAC.

Fig. A3 shows the snapshots at  $t = t_e$ . Clearly, the locations of each vortex core and the size of the primary and secondary vortices are consistent between EMV and SMAC. Fig. A4 shows the velocity profiles at  $x/H = 0.5$  for  $u$  at  $y/H = 0.5$  for  $v$ . These profiles considerably agree between EMV and SMAC, including near each wall where the velocity shear becomes significant. Fig. A5 shows the temporal evolutions of velocity and pressure at the center of cavity ( $x/H = 0.5$  and  $y/H = 0.5$ ). The time evolutions between the two methods show good agreement. Alternatively, the velocity and pressure field simulated by the first-order upwind scheme are considerably different from those simulated by the SMAC with second-order scheme or previous results by Ghia (1982), as shown in Figs. A4 and A5. According to these results, we can conclude that the idea employed in EMV is acceptable for reproducing the velocity and pressure field consistent with those by SMAC. However, we need to consider an appropriate discretization scheme for the advection term due to numerical instability in the explicit numerical simulations.

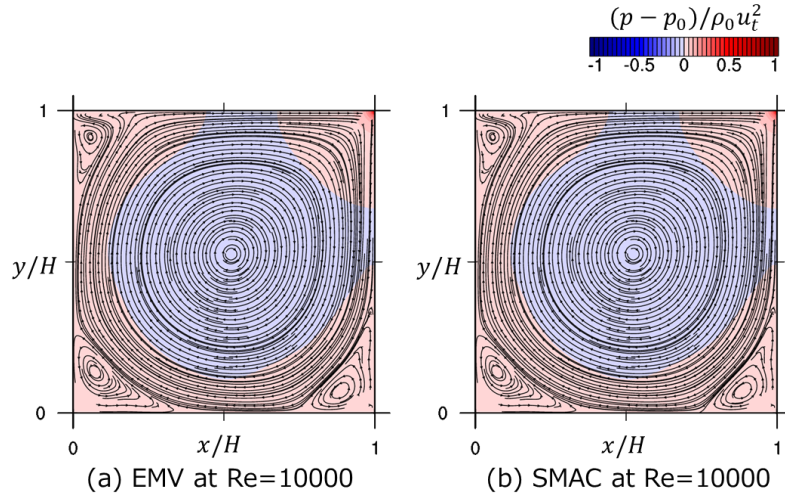


Fig. A3 Streamlines and pressure distributions at  $Re = 10000$  for (a) EMV and (b) SMAC with first-order upwind advection scheme for advection term.

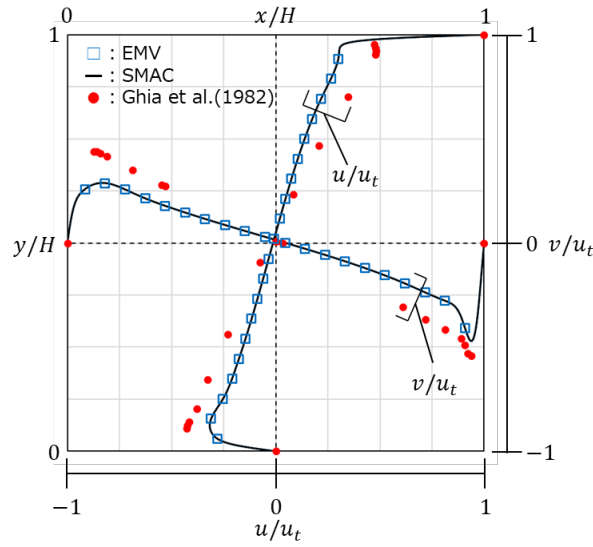
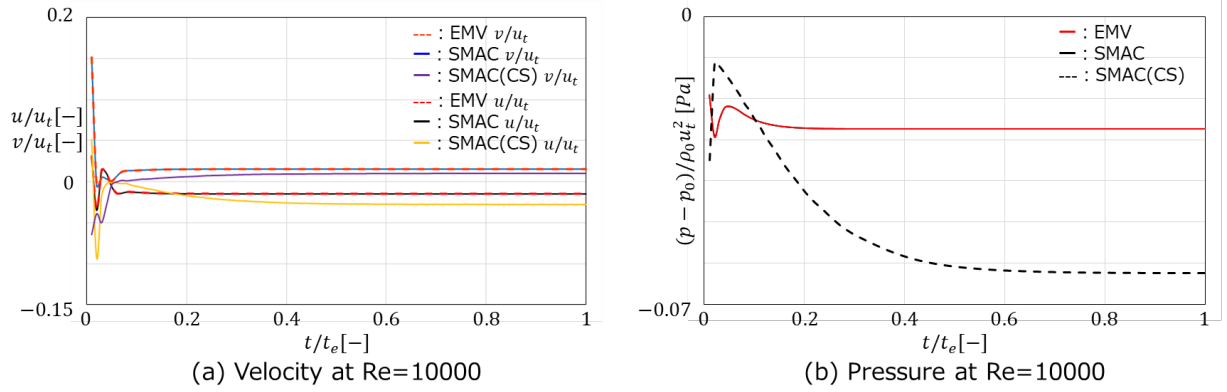


Fig. A4 Velocity profiles in the center lines of cavity for  $u$  at  $x/H = 0.5$  and  $v$  at  $y/H = 0.5$ , for  $Re = 10000$  with the first-order upwind scheme for the advection term. Reference data is after Ghia et al. (1982).



636 Fig. A5 Temporal evolutions of (a) velocity and (b) pressure at center of cavity ( $x/H = 0.5$   
637 and  $y/H = 0.5$ ) for  $Re = 10000$  with the first-order upwind scheme. CS is the  
638 second-order center scheme used for SMAC in Section 3.

639 Nomenclature:  
 640  $a = (dp/d\rho)^{0.5}$ : speed of sound [m/s]  
 641  $c = \Delta/\Delta t$ : representative speed of virtual particle [m/s]  
 642  $\mathbf{c}_i$ : ultra-discrete velocity of virtual particle [m/s]  
 643  $c_p$ : specific heat under isobar condition [J/kgK]  
 644  $c_v$ : specific heat under isochoric condition [J/kgK]  
 645  $D$ : dimension [-]  
 646  $e_{ij} = (\partial u_i/\partial x_j + \partial u_j/\partial x_i)$ : velocity strain tensor [1/s]  
 647  $k$ : thermal conductivity [J/Kms]  
 648  $k_B$ : Boltzmann constant [J/K]  
 649  $m$ : mass of molecule [kg/pcs]  
 650  $N$ : molecule density per unit volume [pcs/m<sup>3</sup>]  
 651  $n$ : amount of substance [mol]  
 652  $N_A$ : Avogadro number [-]  
 653  $p$ : pressure [Pa]  
 654  $p_v$ : pressure by virtual particle impulse [Pa]  
 655  $\mathbf{q}^i$ : velocity of molecule  $i$  [m/s]  
 656  $q_x^i, q_y^i, q_z^i$ : velocity component of molecule  $i$  [m/s]  
 657  $q_T$ : thermal velocity [m/s]  
 658  $\mathbf{q}_v^i$ : velocity of virtual particle  $i$  [m/s]  
 659  $q_{vx}^i, q_{vy}^i, q_{vz}^i$ : velocity component of molecule  $i$  [m/s]  
 660  $q_{vT}$ : thermal velocity defined by virtual particle [m/s]  
 661  $R$ : gas constant [J/kgK] ( $p/\rho = RT$ : ideal gas law)  
 662  $s$ : specific entropy [J/kgK]  
 663  $T$ : temperature [K]  
 664  $t$ : time [s]  
 665  $U$ : internal energy [J]  
 666  $U_v$ : internal energy by virtual particle [J]  
 667  $u_i$ : velocity in tensor notation [m/s]  
 668  $V$ : fluid velocity [m/s]  
 669  $u, v, w$ : velocity in component notation [m/s]  
 670  $x, y, z$ : coordinate in component notation [m]  
 671  $x_i$ : coordinate [m]  
 672  $\alpha = k/\rho c_p$ : thermal diffusivity [m<sup>2</sup>/s]  
 673  $\gamma = c_p/c_v$ : ratio of specific heat [-]  
 674  $\Delta$ : grid spacing [m]  
 675  $\Delta t$ : discrete time [s]  
 676  $\delta_{ij}$ : Kronecker's delta [-]  
 677  $\theta = \partial u_i/\partial x_i$ : divergence of  $u_i$  [1/s]  
 678  $\lambda$ : second dynamic viscosity [kg/ms]  
 679  $\mu$ : dynamic viscosity [kg/ms]  
 680  $\phi$ : dissipation rate [J/m<sup>3</sup>s]  
 681  $\rho, \rho_0, \rho_{max}, \rho_{min}$ : density [kg/m<sup>3</sup>]  
 682  $\Omega$ : volume [m<sup>3</sup>]

# Reference:

- [1] A.J. Chorin, A numerical method for solving incompressible viscous flow problems, *J. Comput. Phys.* 2 (1967) 12–26. [https://doi.org/10.1016/0021-9991\(67\)90037-X](https://doi.org/10.1016/0021-9991(67)90037-X).
- [2] J.L. Steger, P. Kutler, Implicit Finite-Difference Procedures for the Computation of Vortex Wakes, *AIAA J.* 15 (1977) 581–590. <https://doi.org/10.2514/3.60663>.
- [3] P.A. Madsen, H.A. Schäffer, A discussion of artificial compressibility, *Coast. Eng.* 53 (2006) 93–98. <https://doi.org/10.1016/j.coastaleng.2005.09.020>.
- [4] S. Vrahliotis, T. Pappou, S. Tsangaris, Artificial compressibility 3-D Navier-Stokes solver for unsteady incompressible flows with hybrid grids, *Eng. Appl. Comput. Fluid Mech.* 6 (2012) 248–270. <https://doi.org/10.1080/19942060.2012.11015419>.
- [5] J.R. Clausen, Entropically damped form of artificial compressibility for explicit simulation of incompressible flow, *Phys. Rev. E - Stat. Nonlinear, Soft Matter Phys.* 87 (2013) 1–12. <https://doi.org/10.1103/PhysRevE.87.013309>.
- [6] S. Ansumali, I. V. Karlin, H.C. Öttinger, Thermodynamic theory of incompressible hydrodynamics, *Phys. Rev. Lett.* 94 (2005) 1–4. <https://doi.org/10.1103/PhysRevLett.94.080602>.
- [7] S. Borok, S. Ansumali, I. V. Karlin, Kinetically reduced local Navier-Stokes equations for simulation of incompressible viscous flows, *Phys. Rev. E - Stat. Nonlinear, Soft Matter Phys.* 76 (2007) 1–9. <https://doi.org/10.1103/PhysRevE.76.066704>.
- [8] A. Toutant, General and exact pressure evolution equation, *Phys. Lett. Sect. A Gen. At. Solid State Phys.* 381 (2017) 3739–3742. <https://doi.org/10.1016/j.physleta.2017.10.008>.
- [9] A. Toutant, Numerical simulations of unsteady viscous incompressible flows using general pressure equation, *J. Comput. Phys.* 374 (2018) 822–842. <https://doi.org/10.1016/j.jcp.2018.07.058>.
- [10] P. Bigay, G. Oger, P.M. Guilcher, D. Le Touzé, A weakly-compressible Cartesian grid approach for hydrodynamic flows, *Comput. Phys. Commun.* 220 (2017) 31–43. <https://doi.org/10.1016/j.cpc.2017.06.010>.
- [11] U. Frisch, D. D’humieres, B. Hasslacher, P. Lallemand, Y. Ves Pomeau, J.-P.R. Ivet, Lattice Gas Hydrodynamics in Two and Three Dimensions, *Complex Syst.* 1 (1987) 649–707.
- [12] X. He, G.D. Doolen, T. Clark, Comparison of the lattice Boltzmann method and the artificial compressibility method for Navier-Stokes equations, *J. Comput. Phys.* 179 (2002) 439–451. <https://doi.org/10.1006/jcph.2002.7064>.
- [13] J.D. Ramshaw, V.A. Mousseau, Accelerated artificial compressibility method for steady-state incompressible flow calculations, *Comput. Fluids.* 18 (1990) 361–367. [https://doi.org/10.1016/0045-7930\(90\)90027-U](https://doi.org/10.1016/0045-7930(90)90027-U).
- [14] Y.T. Delorme, K. Puri, J. Nordstrom, V. Linders, S. Dong, S.H. Frankel, A simple and efficient incompressible Navier–Stokes solver for unsteady complex geometry flows on truncated domains, *Comput. Fluids.* 150 (2017) 84–94. <https://doi.org/10.1016/j.compfluid.2017.03.030>.
- [15] A. Kajzer, J. Pozorski, Application of the Entropically Damped Artificial Compressibility model to direct numerical simulation of turbulent channel flow, *Comput. Math. with Appl.* 76 (2018) 997–1013. <https://doi.org/10.1016/j.camwa.2018.05.036>.
- [16] T. Ohwada, P. Asinari, Artificial compressibility method revisited: Asymptotic numerical method for incompressible Navier-Stokes equations, *J. Comput. Phys.* 229 (2010) 1698–1723. <https://doi.org/10.1016/j.jcp.2009.11.003>.
- [17] A. Kajzer, J. Pozorski, A weakly Compressible, Diffuse-Interface Model for



- Two-Phase Flows, Springer Netherlands, 2020.  
<https://doi.org/10.1007/s10494-020-00164-8>.
- [18] A.A. Amsden, F.H. Harlow, A simplified MAC technique for incompressible fluid flow calculations, *J. Comput. Phys.* 6 (1970) 322–325.  
[https://doi.org/10.1016/0021-9991\(70\)90029-X](https://doi.org/10.1016/0021-9991(70)90029-X).
- [19] U. Ghia, K.N. Ghia, C.T. Shin, High-Re solutions for incompressible flow using the Navier-Stokes equations and a multigrid method, *J. Comput. Phys.* 48 (1982) 387–411.  
[https://doi.org/10.1016/0021-9991\(82\)90058-4](https://doi.org/10.1016/0021-9991(82)90058-4).
- [20] S.G. Rubin, P.K. Khosla, Navier-Stokes calculations with a coupled strongly implicit method-I. Finite-difference solutions, *Comput. Fluids.* 9 (1981) 163–180.  
[https://doi.org/10.1016/0045-7930\(81\)90023-2](https://doi.org/10.1016/0045-7930(81)90023-2).
- [21] F.H. Harlow, J.E. Welch, Numerical calculation of time-dependent viscous incompressible flow of fluid with free surface, *Phys. Fluids.* 8 (1965) 2182–2189.  
<https://doi.org/10.1063/1.1761178>.
- [22] G.D. van Albada, B. van Leer, W.W. Roberts, A Comparative Study of Computational Methods in Cosmic Gas Dynamics, *Upwind and High-Resolution Schemes.* 108 (1997) 95–103. [https://doi.org/10.1007/978-3-642-60543-7\\_6](https://doi.org/10.1007/978-3-642-60543-7_6).
- [23] S. Chen, H. Chen, D. Martnez, W. Matthaeus, Lattice Boltzmann model for simulation of magnetohydrodynamics, *Phys. Rev. Lett.* 67 (1991) 3776–3779.  
<https://doi.org/10.1103/PhysRevLett.67.3776>.
- [24] P.K. Khosla, S.G. Rubin, A diagonally dominant second-order accurate implicit scheme, *Comput. Fluids.* 2 (1974) 207–209.  
[https://doi.org/10.1016/0045-7930\(74\)90014-0](https://doi.org/10.1016/0045-7930(74)90014-0).